**Rare Metal Materials and Engineering**
Volume, Issue ,
Available online at **www.rmme.ac.cn**

**Cite this article as:** Rare Metal Materials and Engineering,.

DOI: 10.12442/j.issn.1002-185X.20240618

# Effect of pore structure on forming quality and performance of Mg-5Zn magnesium alloy porous bone repair scaffold fabricated by SLM

**Zhao Lun[1], Sun Zhichao[1], Wang Chang[1, 2], Zhang Pengsheng[2], Tang Shuai[1], Zhang Baoxin[3]**

[1] *State Key Laboratory of Solidfication Processing, School of Materials Science and Engineering, Northwestern Polytechnical University, Xi'an 710072, People's Republic of China*

[2] *Shaanxi Key Laboratory of Biomedical Metallic Materials, Northwest Institute for Non-ferrous Metal Research, Shaanxi 710016, Xi'an, China*

[3] *Department of Orthopedic Surgery, The Second Affiliated Hospital of Inner Mongolia Medical University, Hohhot 010050, China*

**Abstract:** Four types of Mg-5Zn porous scaffolds with different pore geometries, including body-centered cubic (BCC), the rhombic dodecahedron (RD), primitive (P), and gyroid (G), were designed and fabricated using SLM. Their forming quality, compression mechanical properties, and degradation behavior were investigated. The results indicate that the scaffolds fabricated exhibited good dimensional accuracy, and the surface chemical polishing significantly improved the forming quality and reduce porosity error in porous scaffolds. Compared to the rod structures (BCC, RD), the surface structures (G, P) scaffolds had less powder particle adhesion. The G porous scaffold exhibited the best forming quality for the same design porosity. The predominant failure mode of scaffolds during compression was a 45° shear fracture. At a porosity of 75%, the compression performance of all scaffolds met the compressive performance requirements of cancellous bone, and BCC and G structures showed relatively better compression performance. Immersed in Hank's solution for 168 hours, the B-2-75% pore structure scaffold exhibited severe localized corrosion, with fractures in partial pillar connections. In contrast, the G-3-75% pore structure scaffold mainly underwent uniform corrosion, maintaining structural integrity, and the corrosion rate and loss of compressive properties are less than those of the B-2-75% structure. After comparison, the G-pore structure scaffold is preferred.

**Key words:** Magnesium alloy porous bone repair scaffold; Selective laser melting; Pore structure; Forming quality; Mechanical property; Degradation performance

Implanting bone repair scaffolds provides a more effective and safer method for treating large-area bone defects. Magnesium alloys possess a low modulus of elasticity and good biodegradability. They can promote bone tissue growth, making magnesium alloy porous bone repair scaffolds broadly promising in application [1-5]. Selective Laser Melting (SLM) is an additive manufacturing technology that melts discrete powder materials and builds them up layer by layer, which can accurately design and efficiently fabricate scaffolds with complex internal pore structures according to the shape of the patient's bone defects to promote cell adhesion, nutrient delivery, and bone tissue regeneration [6-9]. A reasonable magnesium alloy porous scaffold should have good SLM-forming quality, adequate support strength, and favorable degradation behavior to provide a viable environment for recovering and regenerating of damaged bone tissue. However, magnesium alloys are prone to vaporization and spheroidization during SLM processing [10]. The forming quality, mechanical property, and degradation

Foundation item: Science and Technology Planning Project of Inner Mongolia Science and Technology Department(2022YFSH0021); Key Research and Development Program of Shaanxi Province (2024SF2-GJHX-14, 2021SF-296)

Corresponding author: Sun Zhichao, Ph.D., Professor, State Key Laboratory of Solidfication Processing, School of Materials Science and Engineering, Northwestern Polytechnical University, Xi'an 710072, P. R. China, Tel: 0086-29-88460212-802, E-mail: zcsun@nwpu.edu.cn

performance of the scaffolds are sensitive to structural attributes such as pore units and porosity [11]. Mg-5Zn without toxic elements shows a better combination of biocompatibility and mechanical strength[12, 13]. In addition, Mg-5Zn alloy powder for additive manufacturing can be prepared through mature commercialization. Therefore, studying and clarifying the ideal pore structure and properties of degradable Mg-5Zn magnesium alloy scaffolds suitable for the SLM process has a vital role in promoting the development of magnesium alloy porous bone repair scaffolds.

Compared to porous structures with inconsistent structural shapes and irregular, disorganized distribution, regular porous structures with repeated arrangements of the same unit, such as rod unit structures and surface unit structures, exhibit more uniform stress distribution and are less challenging to fabricate using selective laser melting (SLM) [14-16]. Current research on the porous topology design of titanium alloys has rapidly advanced [17-19]. The porous structures used in bone repair play a crucial role in mechanical properties and influence the proliferation and differentiation of cell growth [20-22]. Pore sizes between 60% and 90% are suitable for bone ingrowth. Although an increase in porosity can enhance bone cell integration, it will reduce mechanical properties [23]. Lietaert et al. [24] designed and fabricated porous zinc alloy scaffolds with five different unit structures (diamond, octet truss, 3D Kagome, etc.) with 70% porosity by SLM and found that the 3D Kagome structure exhibited the best yield strength. Li et al. [25] fabricated topologically ordered porous magnesium (WE43) scaffolds based on diamond unit cells and found that they meet bone tissue engineering requirements. Wang et al. [26] designed and fabricated three different structures (biomimetic, diamond, and gyroid) of porous JDBM scaffolds by SLM, and the results showed that the gyroid scaffold had the best performance. Magnesium alloy porous scaffolds gradually degrade during service, which means their porous structure presents more considerations than inert metal scaffolds.

The forming quality and performance of bone-repair porous scaffolds are critical to their application. Xiao et al. [27] utilized topological optimization to achieve a microstructure with maximum stiffness under the constraint of a specific pore volume fraction. When the minimum average pore diameter was 231 μm, the metal scaffolds'3D geometric shape and pore morphology were reproduced with high precision. Xie et al. [28] produced JDBM magnesium alloy porous scaffolds using SLM that exhibited suitable mechanical properties and demonstrated excellent osteoinductivity in vitro. However, a large amount of alloyed spherical powder residue on the surface of the porous scaffolds led to varying degrees of obstruction in the designed structural pores, resulting in a porosity of only 32.1%, significantly lower than the intended design porosity of 80%. Liu et al.[8] studied the WE43 magnesium alloy porous scaffolds fabricated using SLM, and the results showed that the spatial distribution of forming errors in different unit scaffolds varies. Also, the forming quality of the scaffolds is related to the designed porous structure. By designing the porous structure, the mechanical properties of the scaffolds can be extensively adjusted to meet the mechanical performance requirements of cancellous bone.

Appropriate degradability is another critical indicator for implanted bone repair scaffolds. Jia et al. [29] studied magnesium alloy scaffolds with two types of 3D interconnected porous structures. They found that the degradation products were unrelated to the pore structure. During the degradation process, the external pore structures of both scaffolds were gradually obstructed by degradation products, leading to reduced interconnectivity between external and internal pores and varying degradation rates. Li et al. [30] found that the degradation products attached to the magnesium alloy porous scaffolds after degradation have minimal impact on load-bearing. Wang et al. [31] demonstrated that three types of structures (biomorphic, diamond, and gyroid) fabricated via selective laser melting (SLM) exhibited sufficient degradation resistance and compressive performance for WE43 magnesium alloy porous scaffolds, meeting the requirements of bone tissue engineering. However, there are significant differences in the mechanical properties and degradation behavior among the various structured porous scaffolds. The diamond unit-cell porous magnesium alloy scaffold fabricated by SLM maintains its structural integrity after degradation. However, during this process, Young's modulus is affected by changes in the scaffold's internal structure, attributed to localized corrosion-induced stress concentration [25]. The structural unit of porous magnesium alloy scaffolds (JDBM) plays a critical role in influencing compressive mechanical performance, and the degradation rate is directly correlated with the structure of the porous scaffold [26]. From the above study, the structure of magnesium alloy porous scaffolds significantly influences their forming ability, mechanical properties, and degradation performance. Further research is needed to investigate the optimal pore structure, forming quality, and performance of Mg-5Zn scaffolds.

Four typical structures of Mg-5Zn porous scaffolds with varying pore sizes: body-centered cubic (BCC), rhombic dodecahedron (RD), primitive (P), and gyroid (G), based on the structural characteristics of bone repair scaffolds, were designed and fabricated by SLM in this study. Their forming ability, mechanical properties, and degradation performance were investigated, aiming to guide the design and fabrication of Mg-5Zn alloy porous scaffolds for bone repair.

## 1 Experiment

### 1.1 Scaffolds design

According to the structural characteristics of bone repair scaffolds, four types of pore geometries were designed based on the rod unit and face unit structures that are widely used nowadays: body-centered cube (BCC), rhombic dodecahedron (RD), primitive (P), and gyroid (G). The BCC (Fig. 1(a)) and

RD (Fig. 1(b)) structure unit cell sizes are 2×2×2 mm and 3×3×3mm, respectively. The P (Fig. 1(c)) and G (Fig. 1(d)) structure unit cell sizes are 2×2×2mm and 3×3×3mm, respectively. Different porosities are obtained by varying the supporting rods' diameters or the curved surfaces' wall thicknesses. Based on the manufacturing constraints of laser selective melting equipment and the design requirements for bone repair scaffolds, each structure was designed with four different porosity models, ranging from 64% to 91%. The dimensions of the scaffolds were 10×15mm.

Additionally, for each structure, an extra-porous scaffold with a 75% porosity was designed for comparison. The pore unit dimensions were set at 2.5×2.5×2.5mm. A total of 20 models of the scaffolds were modeled, and the specific model design parameters are shown in Table 1 below.

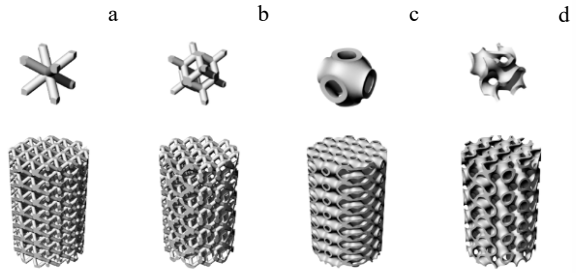


Fig.1 Unit cell structure and 3D modeling of magnesium alloy porous scaffolds: (a) BCC; (b) RD; (c) P; (d) G.

**Table 1 Porous scaffold model parameters**

| Sample Type | number | Rod diameter/Wall thickness（mm） | Porosity |
|---|---|---|---|
| Body-centered cube | B-2-65% | 0.59 | 65% |
| | B-2-69% | 0.54 | 69% |
| | B-2-75% | 0.48 | 75% |
| | B-2-79% | 0.43 | 79% |
| | B-2.5-75% | 0.62 | 75% |
| Rhombic dodecahedron | R-3-70% | 0.58 | 70% |
| | R-3-75% | 0.52 | 75% |
| | R-3-80% | 0.46 | 80% |
| | R-3-85% | 0.39 | 85% |
| | R-2.5-75% | 0.43 | 75% |
| Primitive | P-2-66% | 0.30 | 66% |
| | P-2-70% | 0.26 | 70% |
| | P-2-75% | 0.22 | 75% |
| | P-2-80% | 0.18 | 80% |
| | P-2.5-75% | 0.27 | 75% |
| Gyroid | G-3-70% | 0.30 | 70% |
| | G-3-75% | 0.25 | 75% |
| | G-3-80% | 0.20 | 80% |
| | G-3-85% | 0.15 | 85% |
| | G-2.5-75% | 0.21 | 75% |

### 1.2 Scaffold fabrication and post-processing

The Mg-5Zn powders in this article were prepared by centrifugal atomization (Tangshan Weihao, China). The particle size distribution was mainly 20~80 μm, with an average particle size of 47.68 μm, as shown in Fig. 2. The BLT S210 selective laser melting equipment was used, equipped with a fiber laser with a maximum power of 500W, a spot diameter of 100 μm, and a maximum forming size of 105mm×105mm×200 mm. Based on the previous research on SLM forming of Mg-5Zn alloy, the process parameters were selected: laser power of 70 W, scanning speed of 400 mm/s, scanning spacing of 0.06 mm, and powder layer thickness of 0.03 mm. The scanning strategy involves bidirectional scanning, with the scanning lines staggered by 67° between consecutive layers, and the forming was performed in high-purity argon gas.

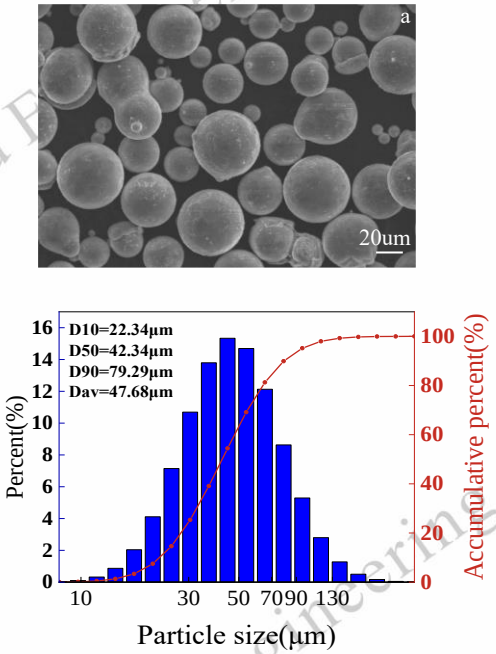


Fig.2 Mg-5Zn powder morphology and particle size distribution: (a) Morphology; (b) Particle size distribution.

After fabrication, all the magnesium alloy porous scaffolds were ultrasonically cleaned for 4 hours. The scaffolds were then chemically polished in a 5%HCl+5%$HNO_3$+90%$C_2H_5OH$ solution for 120 seconds. The polishing process was carried out using a magnetic stirrer at 800 rpm, followed by rinsing with water and anhydrous ethanol and finally drying in a drying oven.

### 1.3 porosity detection and morphological observation

The porosity of the prepared porous scaffold specimens was measured by density balance based on the Archimedes drainage method according to the ASTMB962-08 standard, and anhydrous ethanol was used as the medium instead of water in the

measurement. The macroscopic morphology, microstructures, and fracture morphology of the scaffolds were observed using the Hitachi SU5000 thermal field emission scanning electron microscope. The elemental distribution of the micro-zone organization was analyzed by combining with the Oxford Max Ultim energy spectrometer.

### 1.4 Mechanical properties and failure modes of porous scaffolds

The compression performance of the porous magnesium alloy scaffolds was tested using a CTM8050 electronic universal testing machine. The compression speed was set at 0.9 mm/min, and the compression ratio was 50%. The corresponding yield strength, compressive strength, elastic modulus, and failure mode can be determined by analyzing the engineering stress-strain curve.

### 1.5 Degradation behavior of porous scaffolds

The degradation behavior of porous scaffolds with a porosity of 75% in BCC structure (B-2-75%) and P structure (G-3-75%) was investigated through simulated body fluid (SBF) immersion experiments. The immersion tests follow the ASTM G31-72 standard. Hank's simulated body fluid in the immersion experiments was prepared using Coolaber's dry powder HBSS balanced salt solution. The pH was adjusted to 7.4 at 36.5 ± 0.5 °C. The composition of the simulated body fluid is shown in Table 2.

**Table 2 Simulated body fluid (Hank's) composition (1L)**

| Components | Weight/g |
|---|---|
| NaCl | 8.000 |
| KCl | 0.350 |
| Na2HPO4 | 0.400 |
| KH2PO4 | 0.060 |
| MgSO4 | 0.098 |
| CaCl2 | 0.140 |
| Na2SO4 | 0.072 |
| Glucose | 1 |

PH measurements and the weight loss method were used to characterize the corrosion rate of porous magnesium alloy scaffolds in Hank's solution. (1) the pH of the 500 ml of simulated body fluid containing the porous scaffold was measured at set intervals for pH testing. The scaffold was temporarily removed to prevent changes in pH during the test. Before testing, calibrate the pH meter and ensure the simulated body fluid is stirred uniformly. The pH electrode should be rinsed with deionized water and dried with filter paper before each measurement. Read the pH value once the reading stabilizes. (2) For the weight loss test, immerse the sample in a chromic acid solution (CrO3: 200 g/L, AgNO3: 10 g/L). After soaking, use ultrasonic cleaning for 5 minutes to remove corrosion products, followed by rinsing with deionized water. Clean the sample thoroughly in anhydrous ethanol to remove any residual chromic acid solution from the surface, then dry it before weighing. The corrosion rate of the porous scaffolds was calculated according to the ASTM G31-72 standard using the following formula:

$$CR = \frac{K*W}{A*T*D} \quad (1)$$

In the formula, CR represents the corrosion rate, measured in mm/year; K is a constant, with a value of $8.76 \times 10^4$; W denotes the weight loss before and after immersion, measured in grams; A stands for the surface area of the immersed sample, measured in $cm^2$; T represents the immersion time, measured in hours; and D signifies the density of the immersed sample, measured in $g/cm^3$.

Simultaneously, the compression performance loss rates of the two types of pore structure scaffolds after immersion in Hank's solution for 168 hours were statistically analyzed, and the corresponding mechanical performance losses were calculated.

## 2 Results and discussion

### 2.1 Forming quality of porous scaffolds

Figure 3 shows the surface morphology of the four structural porous scaffolds (BCC, RD, G, and P) fabricated by SLM. Before and after chemical polishing, the fabricated magnesium alloy porous scaffolds closely match the 3D models in Figure 1. Before chemical polishing, the four types of porous scaffolds, exhibit overall intact and uniform structures but suffer from significant powder adhesion and partial pore blockage. After chemical polishing, the structural morphology of the scaffolds was clearly presented, with a smooth and dense surface without apparent defects and a metallic luster. The metallographic microstructure of the four structural porous scaffolds is shown in Fig. 4, which is mainly composed of equiaxed grains and fewer columnar grains at the melt pool boundaries. The grains are uniformly refined overall, ranging from 4 to 13 μm in size. The primary purpose of the chemical polishing process is to remove a large amount of unmelted spherical powder from the surface of the porous scaffolds and to reduce the roughness of the scaffold surface and improve the surface-forming quality.

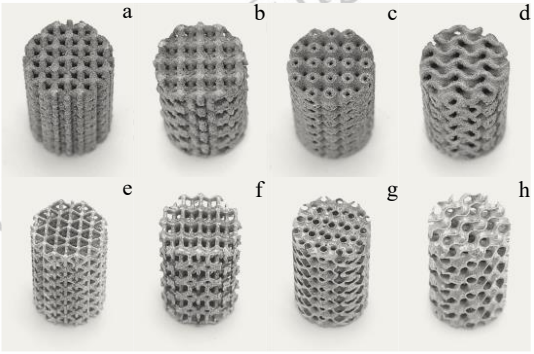


Fig.3 Photographs of four porous magnesium alloy scaffolds before and after chemical polishing: (a), (e) BCC; (b), (f) RD; (c), (g) P; (d), (h) G

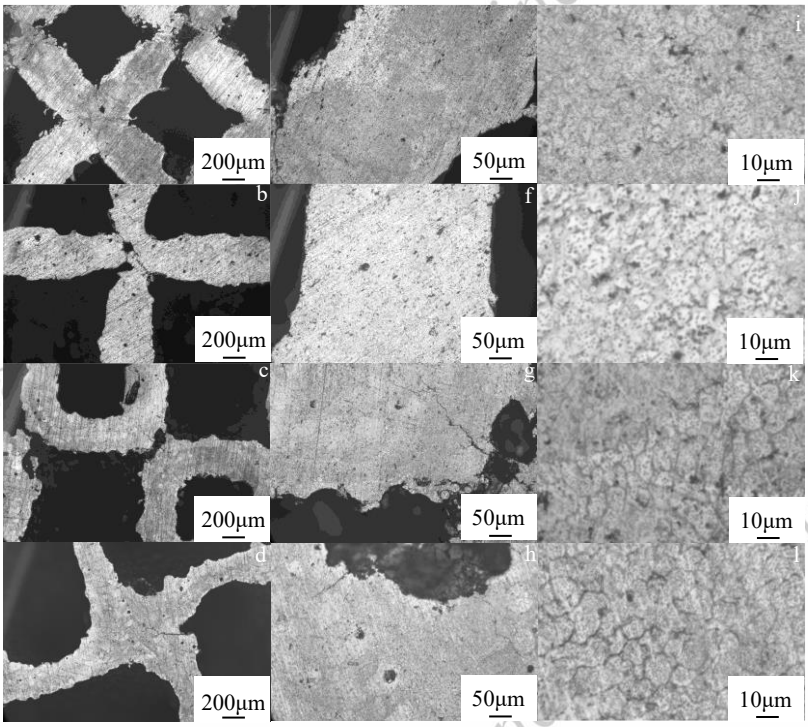


Fig.4 Metallographic microstructures of four kinds of scaffolds: (a), (e), (i) BCC; (b), (f), (j) RD; (c), (g), (k) P; (d), (h), (l) G.

To further observe the surface morphology and polishing effect of the porous scaffolds, SEM observations and analyses were conducted on the top and side surfaces of the four types of scaffolds, as shown in Figure 5. The number of powder particles adhered to the surface of the scaffolds before polishing was large, with different shapes and sizes. The depths of the particles incorporated into the support structure varied, leading to various degrees of pore blockage in the designed structure. As shown by the top morphology of the scaffolds (Fig. 5(a), (e), (i), and (m)), the adhered powder on the surface structure scaffolds is more uniform compared to the rod structure scaffolds, resulting in the overall shape of the scaffold being closer to the design. The adherent powders on the surface of the rod unit RD structure lead to severe pore blockage (Fig. 5(e)). From the morphology of the scaffold's side view (Fig. 5(c), (g), (k), (o)), it is evident that the powder adhered to the sides of the four types of porous scaffolds is significantly greater than that on the top. Additionally, since parts of the side holes of the scaffold are suspended, the powder adhered to the surface accumulates in clumps at the unsupported, suspended areas (indicated by the red elliptical line in Fig. 5(g)).

After chemical polishing, the powders adhered to the surface of the porous scaffolds are corroded and removed, resulting in surface features that closely resemble the design models and a significant improvement in surface quality (Fig. 5(b), (f), (j), (n), (d), (h), (l), and (p)). As for the top surface, there is no significant difference between the periphery and the center of the scaffolds, and the rod diameter or wall thickness and the pore morphology are relatively good. Among them, the gyroid (G) pore structure exhibits the best quality after polishing (Fig. 5(n)). The connection areas of the rod unit BCC and the rod unit RD scaffolds are coarser compared to the middle part of the rod, resulting in poorer uniformity of the scaffolds (Fig. 5(b), (f)). Similar issues also appeared on the top surface. Some accumulated powder particles that were not completed corroded and removed still remain at the rod connections or hanging positions, such as in the "valley" area of the P structure surface (Fig. 5(l)). In a comprehensive comparison of surface roughness, residual powder, and uniformity, the G-structure porous scaffolds are better than those of the other three types of porous structure s.

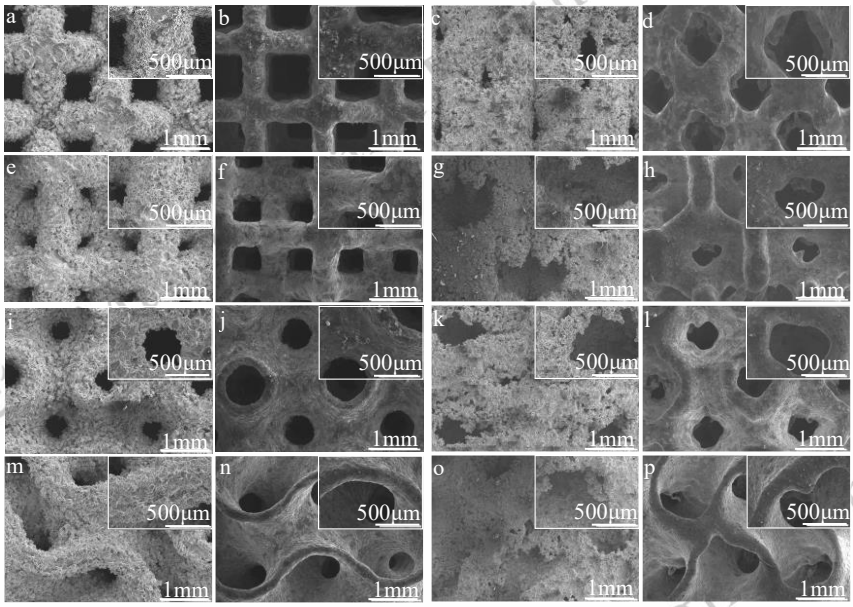


Fig.5 Top and side SEM images of four porous scaffolds before and after polishing. Top surface: (a), (b) BCC; (e), (f) RD; (i), (j) P; (m), (n) G. Lateral side: (c), (d) BCC; (g), (h) RD; (k), (l) P; (o), (p) G.

Fig. 6 shows the results of comparing the measured porosity values of the magnesium alloy porous scaffolds and the design model values, which denote the porosity error data. As shown in Figure 6(a), it can be seen that the porosity errors of the four types of pore structure scaffolds are between 20% and 30% before chemical polishing. When the unit cell size is 3 mm, the porosity error decreases with increasing porosity. When the porosity is 75%, the porosity error decreases with increasing unit cell size. As the rod diameter or wall thickness increases, the porosity error decreases. After chemical polishing, the porosity error of most porous scaffolds can be reduced to around 10%. For the same pore geometry scaffold, the unit cell size is larger, and the error is smaller after polishing. From Figs. 5 and 6, it can be found that the appropriate chemical polishing process can effectively reduce the pore error of porous scaffolds and the surface roughness of porous scaffolds to improve the porosity of the porous scaffolds. However, due to the structure, forming process and forming characteristics of porous scaffolds, chemical polishing can't eliminate the forming error of the scaffolds. Of course, chemical polishing may also lead to over-polishing in some regions of porous scaffolds of different structures, which may, on the contrary, make the porous scaffolds susceptible to stress concentration in the over-polished regions when subjected to force or increase the degradation rate of the area, leading to premature failure of the porous structure.

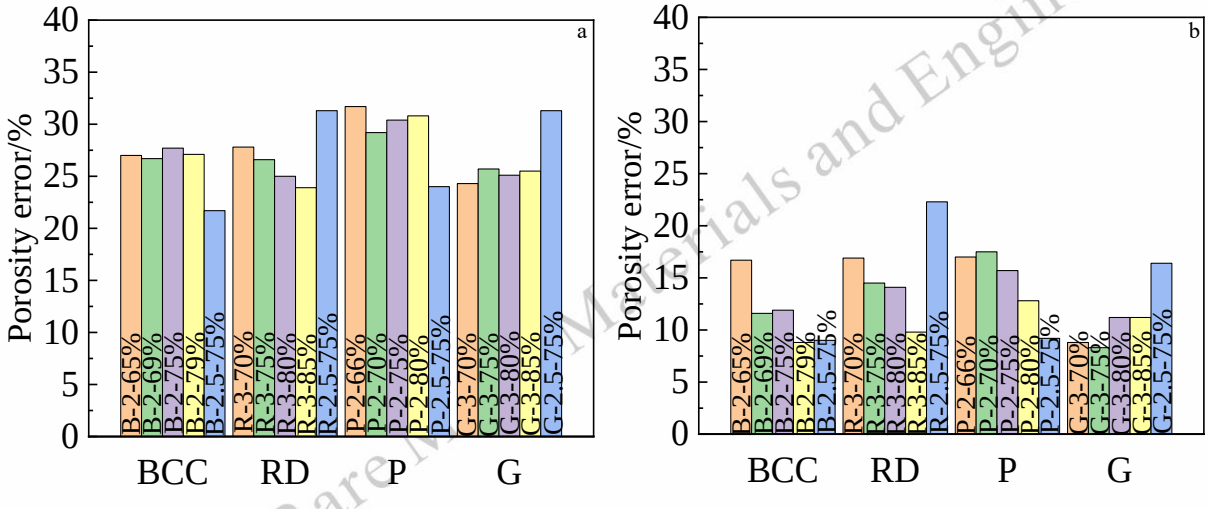


Fig.6 Porosity error of magnesium alloy porous scaffolds: (a) Before chemical polishing; (b) After chemical polishing.

The above analysis indicates that for magnesium alloy porous scaffolds fabricated by SLM, there is a significant amount of spheroidized powder residue on the surface and varying degrees of blockage of the structural pores. This can be effectively improved by post-processing through chemical polishing. However, some powder residue remains at the rod connections or dangling positions. Chemical polishing can enhance the surface quality of the scaffolds and improve the porosity of porous scaffolds. However, it does not fundamentally eliminate forming errors. Excessive chemical polishing also negatively affects the scaffolds' mechanical properties and degradation behavior. The pore structure is a crucial factor affecting the forming quality of the scaffolds. Regardless of before or after polishing, the degree of powder adhesion and the forming error are lower for surface-structure scaffolds than rod-structure scaffolds. For BCC and RD structures, as the porosity increases, the size of the rods decreases, leading to difficulties in forming. After chemical polishing, the surface roughness, powder residue, and uniformity of G-structure porous scaffolds are superior to the other three structures. Under the same porosity conditions, the forming quality of G-structure scaffolds is the best.

## 2.2 Mechanical properties of porous scaffolds

The mechanical properties and compressive failure modes of four porous scaffolds with different porosities after polishing treatment were investigated by quasi-static compression experiments. Figure 7 shows the compressive stress-strain curves of the porous scaffolds, which present the typical compressive deformation characteristics of porous structures, where the stresses rapidly rise to a higher point first, followed by oscillations with deformation.

The stress-strain curves of the four structures show weak fluctuations in the inelastic phase before reaching the compressive strength, which may be caused by the localized minor fragmentation of the porous structure before reaching the maximum stress. There are differences in the compressive stress-strain curves of different porous structures, and the rod unit structure stress exhibits violent vibration with strain when reaching the structural damage (Fig. 7(c), (d)). In contrast, the surface unit structure shows a more moderate magnitude of stress variation with strain (Fig. 7(c), (d)). The compressive strength is higher for the BCC structure with rod units and the G structure with face units. For the same type of porous structure, the stress-strain curves are shifted downward with increasing porosity, indicating that as porosity increases, the yield strength, compressive strength, and elastic modulus of the porous structure decrease. For scaffolds with a consistent porosity of 75% with the same type of structural model, the initial peak stress on the compression curve decreases with increasing unit cell size. However, as the unit cell size diminishes, the challenge of acid-etching the scaffold intensifies, resulting in more significant porosity errors, which can also impact mechanical properties.

Based on the compression curves of scaffolds designed with a porosity of 75%, the compressive strengths and elastic moduli were obtained for B-2-75% (actual porosity = 65.5%), R-3-75% (actual porosity = 60.5%), P-2-75% (actual porosity = 59.3%), and G-3-75% (actual porosity = 66.7%). The compressive strengths were 63.5 MPa, 27.5 MPa, 28.5 MPa, and 40.0 MPa, respectively, while the elastic moduli were 1231±10 MPa, 807±2 MPa, 1212±9 MPa, and 1358±5 MPa. BCC and G structures exhibited superior compression performance among these structures compared to RD and P structures, with the G structure demonstrating stronger resistance to elastic deformation.

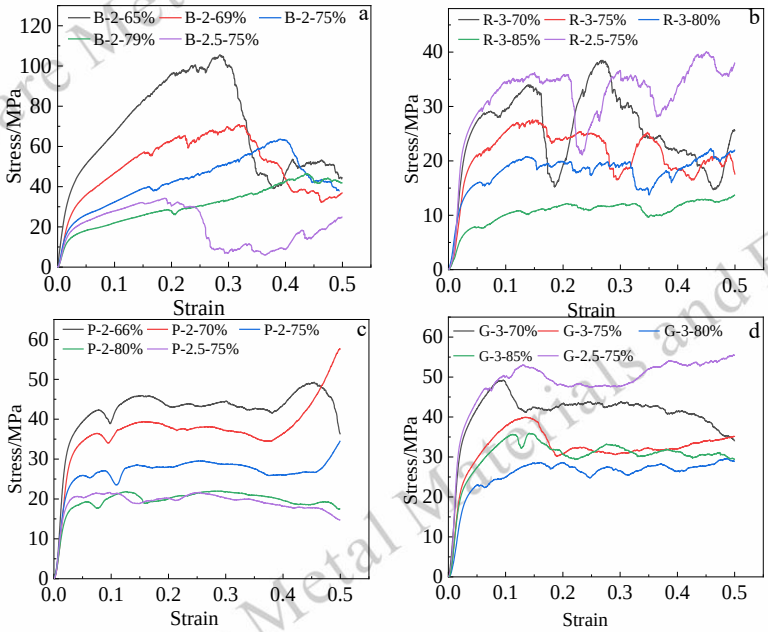


Fig.7 Stress-strain curves of magnesium alloy porous scaffolds: (a) BCC; (b) RD; (c) P; (d) G.

Figure 8 shows the failure modes of the porous scaffolds at a compression strain of 50%, exhibiting three failure modes: 45°

shear failure, fragmentation, and interlayer collapse. The predominant failure mode is the 45° shear failure, closely related to the porous structure. BCC and RD structures primarily experience 45° shear fracture (Fig. 8(a), (b)), with localized fragmentation, particularly evident in the RD structure. The primary failure mode of the P structure varies with porosity. At a porosity of 49%, 45° shear failure occurs (Fig. 8(c)); at a porosity of 52.5%, both 45° shear failure and interlayer collapse are observed (Fig. 8(d)); when the porosity exceeds 59.3%, the specimen is flattened, resulting in interlayer collapse (Figure 8(e)). The G structure exhibits typical 45° shear failure. However, the shear band bends, possibly due to stress concentration at certain angles during loading.

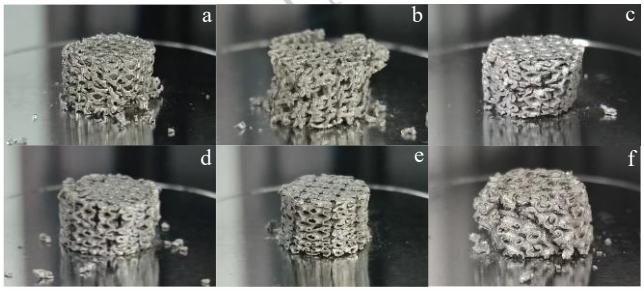


Fig.8 Compression failure mode of porous scaffolds: (a) BCC; (b) RD; (c-e) P; (f) G.

During the compression of various porous structures, the stress undergoes stages of linear increase, nonlinear increase, oscillation, and densification [25]. Before reaching the first peak, the stress exhibits slight fluctuations, indicating local fragmentation within the porous structure, which could be related to local defects in the scaffold. The compressive performance of the four structures of porous scaffolds discussed in this paper meets the requirements for cancellous bone, whose compressive strength and Young's modulus range from 0.2 to 80 MPa and 0.01 to 2 GPa, respectively[26, 32]. At the same designed porosity (75%), the BCC porous structure and G-porous structure exhibit better compressive mechanical properties, while increasing porosity leads to reduced compression performance for the same structure. 45° shear fractures predominantly characterize the compression failure modes of BCC, RD, and G structures. In contrast, the failure mode of the P structure varies with porosity.

### 2.3 Analysis of the degradation properties of porous scaffolds

Bone repair scaffolds with porosity in the range of 70~80% exhibit good osteogenic properties, so BCC (B-2-75%) and G (G-3-75%) structure porous scaffolds with a porosity of 75% were selected for the analysis of degradation properties. Figure 9 shows the results of the pH change curves, weight loss rates, corrosion rates, stress-strain curves, and mechanical performance loss results of the porous scaffolds over various immersion times in Hank's solution. Initially, the pH in Hank's solution rises rapidly, stabilizing after 12 hours, with the B-2-75% structure showing a slightly higher pH than the G-3-75% structure during the immersion period (Fig. 9(a)). After 168 hours of immersion, the weight loss rates for B-2-75% and G-3-75% are 31.7% and 30.0%, respectively, with corrosion rates of 3.66 mm/year and 2.83 mm/year (Fig. 9(b)). The weight loss and corrosion rate calculations for both structures are consistent with the trend in pH change, with the G-3-75% scaffold having a slightly lower corrosion rate than the B-2-75% structure, which is related to the quality of scaffold formation and structural characteristics.

After immersion, the compression stress-strain curves and mechanical performance loss of the two types of scaffolds are shown in Fig. 9(c) and (d). The stress-strain curves of the scaffolds overall decreased. For the B-2-75% scaffold, the yield strength post-immersion is 5.9 MPa, the compressive strength is 31.5 MPa, and the elastic modulus is 508±5 MPa. In contrast, the G-3-75% scaffold has a yield strength of 14.5 MPa, a compressive strength of 24.9 MPa, and an elastic modulus of 1095±5 MPa. The B-2-75% scaffold exhibits a more significant compressive performance loss than the G-3-75% scaffold. The loss rates of yield strength, compressive strength, and elastic modulus for the B-2-75% scaffold exceed 50%, indicating a significant deterioration in compressive properties.

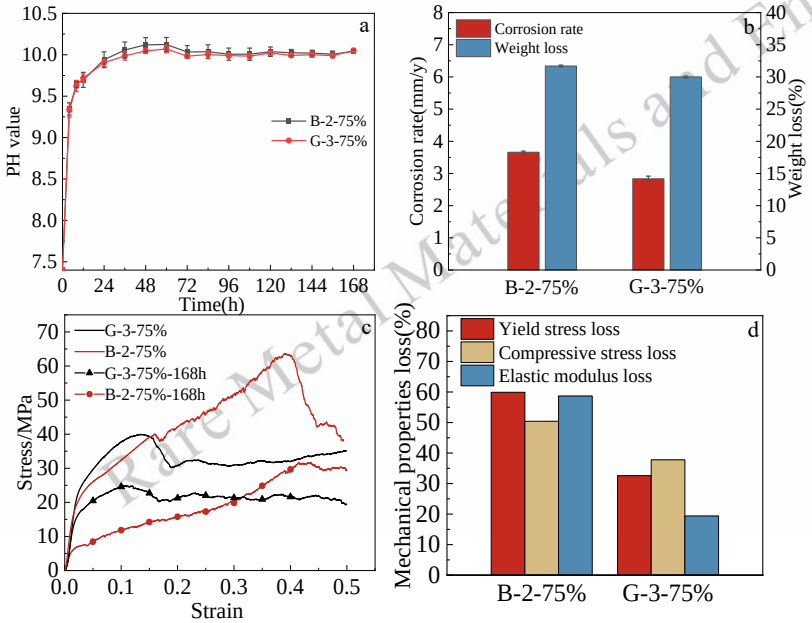

Fig.9 (a) PH change curve of the scaffolds during immersion in Hank's solution; (b) Weight loss and the calculated corrosion rate of the scaffolds in Hank's solution for 168 hours; (c) Compressive stress-strain curve of the scaffolds before and after 168 hours of immersion; (d) Loss of mechanical properties of the scaffolds before and after immersion for 168 hours.

Fig. 10 shows the degradation behavior of B-2-75% and G-3-75% scaffolds. From the macroscopic morphology of the two scaffolds before and after immersion, as demonstrated in Fig. 9 (a), (b), and (c), it can be observed that the scaffolds were darkened. The surfaces were covered with corrosion products after 168 hours of immersion. The white corrosion products partially blocked the pore structure of the scaffolds. Although the overall structure and volume did not change significantly, localized damage occurred (Fig. 10(b)). After removing the degradation products from the surface of the scaffolds, it was found that the pore structure of the B-2-75% scaffold became inhomogeneous and less intact due to localized fractures or even detachment of the rod structure. In contrast, the face unit of the G-3-75% scaffold remained relatively intact, with a visible pore structure. Only the peripheral ends of the structure suffered varying degrees of corrosion damage (Fig. 10(c)).

Fig. 10(d-g) displays the microstructural morphology of the corrosion products after 168 hours of immersion in Hank's solution. Both types of scaffold structures and their pores are covered to varying extents with corrosion products. Compared to the G-3-75% structure (Fig. 10(f)), the B-2-75% structure shows a more significant accumulation of corrosion products around the pores (Fig. 10(d)). Upon closer inspection, it is evident that the corrosion products loosely cover the scaffold surface, especially near the pore structures. Large chunks of corrosion products are present with gaps and cracks between them and the scaffold surface (Fig. 10(e), (g)), indicating a poor integration of the corrosion products with the scaffold matrix.

Fig. 10(h-k) shows the microstructural appearance after removing corrosion products. The B-2-75% structure exhibits fractures at some rod unit junctions, with severe localized corrosion (Fig. 10(h-i), highlighted by red elliptical areas). In contrast, the G-3-75% structure experiences relatively uniform corrosion, maintaining good integrity of its face unit structure without being penetrated or fractured (Fig. 10(f-k)). Both structures display uniformly distributed micro-pitting on their surfaces, which demonstrating the characteristic features of pitting corrosion. This is due to micro-galvanic corrosion occurring between the α-Mg matrix and the second phase present in the materials.

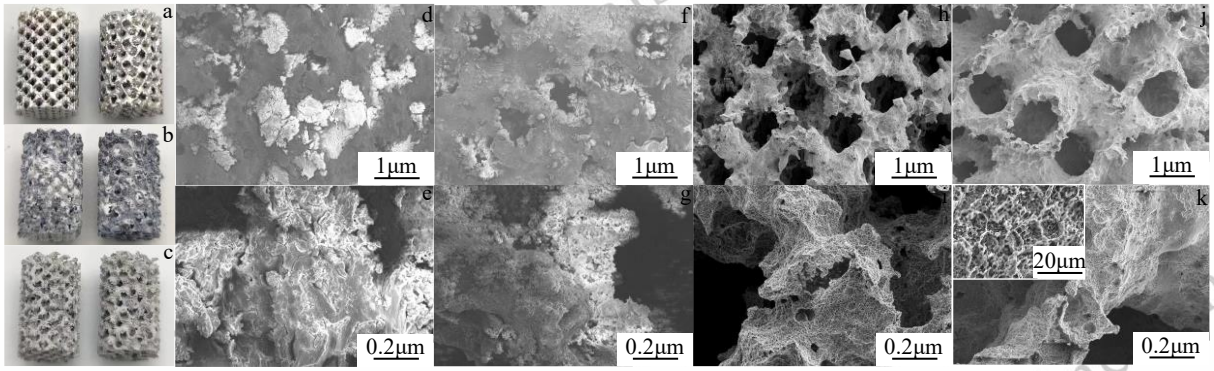


Fig.10 Surface morphology of scaffolds: (a) Before immersion; (b),(d),(e),(f),(g) After 168 hours immersion; (c),(h),(i),(j),(k) Corrosion products removed; Enlarge images: (d), (e), (h), (i) BCC; (f), (g), (i), (k) G.

The microstructural surface morphology and corrosion products of the G-3-75% structure after Hank's immersion for 168 hours were analyzed, as shown in Fig. 11, which reveals that the degradation products mainly consist of two layers. The inner layer is in contact with the substrate. Its surface exhibits numerous cracks and forms fragmented plates. In contrast, the outer layer adheres to the surface of the inner layer, predominantly comprising white, clustered, spherical particles (Fig. 11(a)). Elemental distribution analysis of the corrosion products on the scaffold surface via EDS mapping revealed the presence of O, Mg, P, Ca, Cl, and Zn as the main elements (Fig. 11 (b-c)). The Mg and Zn elements are inferred to originate from the Mg-5Zn magnesium alloy substrate of the scaffold, while the O, P, Ca, and Cl elements are inferred to originate from Hank's solution. The EDS spectra results from regions points 1, 2, and 3 of the degradation products indicate that the atomic ratio of Mg to O in the inner layer at point 1 is approximately 2:1, with less content of Ca and P elements. The main component of the inner corrosion layer is $Mg(OH)_2$, which is relatively dense and can serve as a protective barrier for further corrosion. In the outer layer at point 2, there is a higher ratio of O to Mg atoms, suggesting that the main component is also $Mg(OH)_2$, with a significant amount of chlorine elements, indicating that the corrosion product $Mg(OH)_2$ is reacting with $Cl^-$. At point 3, in addition to O atoms, the content of Ca and P atoms is higher. In comparison, the content of Mg atoms is significantly lower

compared to other regions, suggesting that the composition is mainly composed of calcium phosphate.

The above results indicate that, when immersed in Hank's solution, the macroscopic degradation behavior of BCC and G structure scaffolds with the same porosity is different. However, on a microscopic level, they exhibit predominantly uniform corrosion, resulting in uniform corrosion pits. The B-2-75% structure scaffold exhibited higher pH values, mass loss rates, and corrosion rates than the G-3-75% structure scaffold. The B-2-75% structure also experienced a loss rate exceeding 50% in yield strength, compressive strength, and elastic modulus, indicating more severe mechanical property degradation. This is primarily attributed to differences in degradation rates caused by scaffold structure and surface area[26, 31] . Although the degradation products are unrelated to the porous structure, the external pore structure of both scaffolds gradually becomes obstructed by degradation products , leading to decreased interconnectivity between external and internal pore structures and varying degradation rates [29] . The B-2-75% structure exhibited more corrosion products on its surface and around pores, with severe localized corrosion occurring at some pillar connections, which could lead to pillar fracture or detachment, resulting in significant compression performance loss. In contrast, the smoother geometric transitions of the G-3-75% structure led to relatively uniform corrosion, better integrity of the wall structure, and no corrosion penetration or fracture, resulting in relatively minor compression performance loss. The pore structure directly affects the degradation behavior of porous scaffolds and indirectly influences degradation through its impact on forming quality.

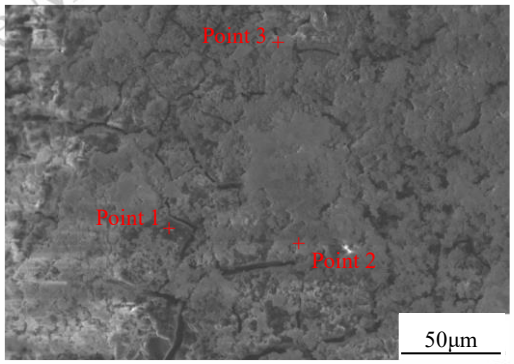


a

| Element (at.%) | Point1 | point2 | point3 |
|---|---|---|---|
| O | 66.72 | 66.74 | 52.80 |
| Mg | 24.30 | 20.79 | 14.57 |
| P | 4.25 | 4.25 | 13.63 |
| Ca | 3.68 | 3.06 | 16.39 |
| Cl | 0.87 | 4.51 | 2.25 |
| Zn | 0.18 | 0.64 | 0.37 |

b

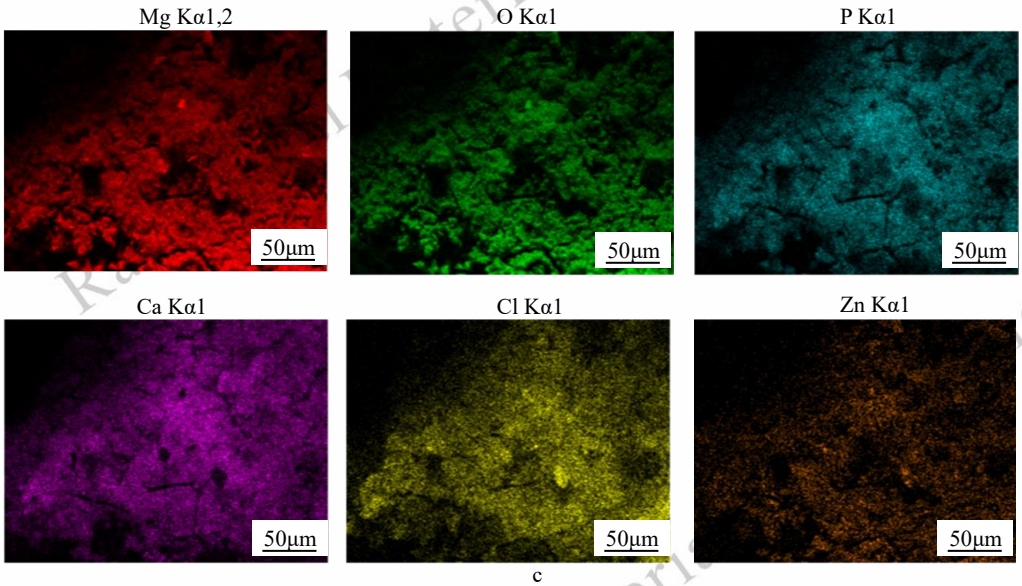


c

Fig.11 The distribution and content of main elements on the corrosion surface of G-3-75% structure scaffolds

## 3 Conclusions

According to the structural characteristics of bone repair scaffolds, four types of Mg-5Zn porous scaffolds with different porosities, including body-centered cubic, rhombic dodecahedron, gyroid, and primitive, were designed and fabricated through selective laser melting (SLM). The forming quality, mechanical properties, and degradation performance of porous scaffolds with different pore structures were investigated.

1) The Mg-5Zn porous scaffolds fabricated by SLM exhibited overall integrity and uniformity. However, severe powder adhesion was observed on the surface, with partial pore

blockage. After chemical polishing, the structural morphology of the porous scaffolds was clearly presented. The surface structure (G, P) scaffolds have less powder adhesion and more minor forming errors than the rod structure (BCC, RD) scaffolds. Among scaffolds with the same design porosity, the G-pore geometry scaffolds showed the best forming quality.

2) The four types of porous structure scaffolds showed typical compressive deformation characteristics of porous structures, and all meet the performance requirements of cancellous bone. The failure mode of the scaffolds in compression was dominated by 45° shear fracture. P-structure scaffolds shifted from 45° shear fracture to interlayer collapse as the porosity increased from 49% to 52.5%. The BCC and G structure had better compressive mechanical properties with the same design porosity, and the compressive properties decreased with increasing scaffold porosity in the same structure.

3) Immersed in Hank's solution for 168 hours, the scaffolds exhibited primarily pitting corrosion, resulting in uniform corrosion pits. The G-3-75% structure scaffolds had relatively more uniform corrosion and slower degradation, better wall structural integrity and less loss of compressive performance due to smoother geometric excesses. In contrast, the B-2-75% structural scaffolds experienced severe local corrosion and partial pillar fracture, significantly losing compression mechanical properties.

In summary, the G-pore structure has excellent structural characteristics, resulting in the best overall performance in forming quality, compressive mechanical properties, and degradation behavior. Therefore, the G-pore structure scaffold is preferred.

## References


1 DebRoy T, Wei H L, Zuback J S et al. *Progress in Materials Science*[J],2018,92: 112

2 Ng C C, Savalani M M, Man H C et al. *Virtual and Physical Prototyping*[J],2010,5(1): 13

3 Shuai Cijun, Yang Youwen, Wu Ping et al. *Journal of Alloys and Compounds*[J],2017,691: 961

4 Wei Kaiwen, Gao Ming, Wang Zemin et al. *Materials Science and Engineering: A*[J],2014,611: 212

5 Esmaily M, Zeng Z, Mortazavi A N et al. *Additive Manufacturing*[J],2020,35: 101321

6 Wysocki B, Idaszek J, Szlązak K et al. *Materials (Basel)*[J],2016,9(3):197

7 Bozkurt Yahya, Karayel Elif. *Journal of Materials Research and Technology*[J],2021,14: 1430

8 Liu Jinge, Liu Bingchuan, Min Shuyuan et al. *Bioactive Materials*[J],2022,16: 301

9 Qin Yu, Wen Peng, Voshage Maximilian et al. *Materials & Design*[J],2019,181: 107937

10 Liu Shuai, Guo Hanjie. *Materials*[J],2020,13(16): 3632

11 Zhang M, Lin R, Wang X et al. *Science Advance*[J],2020,6(12): eaaz6725

12 Jiang Pingli, Blawert Carsten, Zheludkevich Mikhail L et al. *Corrosion and Materials Degradation*[J],2020,1:92

13 Asadollahi Mohammad, Gerashi Ehsan, Alizadeh Reza et al. *Journal of Materials Research and Technology*[J],2022,21: 4473

14 Cai Shuhua, Lei Ting, Li Nianfeng et al. *Materials Science and Engineering: C*[J],2012,32(8): 2570

15 Zadpoor A A. *Journal of Materials Chemistry B*[J],2019,7(26): 4088

16 Zhang Jianguo, Wang Guan, Chen Peng et al. *Rare Metal Materials and Engineering*[J],2023,52(12): 4029

17 Pesode Pralhad, Barve Shivprakash. *Bioprinting*[J],2023,36: e00318

18 Song Changhui, Liu Lisha, Deng Zheng-hua et al. *Rare Metal Materials and Engineering*[J],2023: 2626

19 Fan Yongxia, Lin Yan, Ao Qingbo et al. *Rare Metal Materials and Engineering*[J],2023,52(10): 3630 (in Chinese)

20 Guo Liyao, Ataollah Naghavi Seyed, Wang Ziqiang et al. *Materials & Design*[J],2022,216: 110552

21 Van Bael S, Chai Y C, Truscello S et al. *Acta Biomaterialia*[J],2012,8(7): 2824

22 Deng F, Liu L, Li Z et al. *Journal of Biological Engineering*[J],2021,15(1): 4

23 Bobbert F S L, Lietaert K, Eftekhari A A et al. *Acta Biomaterialia*[J],2017,53: 572

24 Lietaert Karel, Zadpoor Amir Abbas, Sonnaert Maarten et al. *Acta Biomaterialia*[J],2020: 289

25 Li Y, Zhou J, Pavanram P et al. *Acta Biomaterialia*[J],2018,67: 378

26 Wang Yinchuan, Fu Penghuai, Wang Nanqing et al. *Engineering*[J],2020,6(11): 1267

27 Xiao Dongming, Yang Yongqiang, Su Xubin et al. *Transactions of Nonferrous Metals Society of China*[J],2012,22(10): 2554

28 Xie K, Wang N, Guo Y et al. *Bioactive Materials*[J],2022,8: 140

29 Jia Gaozhi, Chen Chenxin, Zhang Jian et al. *Corrosion Science*[J],2018,144: 301

30 Li Y, Jahr H, Pavanram P et al. *Acta Biomaterialia*[J],2020,101: 646

31 Wang Chaoxin, Min Shuyuan, Liu Jinge et al. *Journal of Magnesium and Alloys*[J],2023.

32 Yusop A H, Bakir A A, Shaharom N A et al. *International Journal of Biomaterials*[J],2012: 641430

# 不同构型 Mg-5Zn 镁合金多孔骨修复支架 SLM 成形质量与性能

赵伦[1]，孙志超[1]，王昌[1,2]，张鹏省[2]，汤帅[1]，张葆鑫[3]

（[1]西北工业大学 材料学院 凝固技术国家重点实验室，陕西 西安 710072）

（2 西北有色金属研究院 陕西省医用金属材料重点实验室，陕西 西安 710016）

（3 内蒙古医科大学第二附属医院 骨科，内蒙古 呼和浩特 010050）

**摘　要**：本文设计并通过 SLM 技术制备了体心立方（BCC）、菱形十二面体（RD）、面结构 Gyroid（G）、Primitive（P）四种 Mg-5Zn 多孔支架，研究了其成形质量、压缩力学性能和降解行为。结果表明所制备的支架具有较好的还原度，表面化学抛光处理显著改善了支架成形质量,并降低多孔支架的孔隙误差。面结构（G, P）支架粘附粉末的程度较杆结构(BCC, RD)轻，成形误差较小。相同设计孔隙率下，G 构型支架的成形质量最佳。压缩时支架的失效模式以 45°剪切断裂为主；孔隙率为 75%时，四种构型支架的压缩性能都满足松质骨的压缩性能要求，BCC 和 G 构型支架压缩性能相对较好。Hank's 溶液浸泡 168h， B-2-75%构型支架局部腐蚀较为严重、部分支柱连接处发生断裂，G-3-75%构型支架以均匀腐蚀为主，结构保持较为完整，腐蚀速率和压缩性能损失小于 B-2-75%结构；经综合对比优选 G 构型。

**关键词**：镁合金多孔骨修复支架；激光选区熔化；孔隙结构；成形质量；力学性能；降解性能

---

作者简介：赵伦，男，1998 年生，硕士生，西北工业大学材料学院凝固技术国家重点实验室，陕西 西安 710072，E-mail: zhaolun0009@163.com